RESEARCH   **Open Access**

CrossMark

Exclusive and efficient excitation of plasmonic breathing modes of a metallic nanodisc with the radially polarized optical beams

Mengjun Li[1], Hui Fang[2*] , Xiaoming Li[2] and Xiaocong Yuan[2]

Abstract

Background: The plasmonic breathing modes of a metallic nanodisc are dark plasmonic modes and thus also have the advantage of much smaller radiation loss. These modes emerged previously in electron energy loss spectroscopy experiments and were then pursued with optical excitation methods.

Results: In this paper, through the finite element method type numerical simulations, we show evidence of the pure excitation of these modes under the illumination of two counter-propagating, radially-polarized optical beams. The obtained near-field spectrum of a single Au or Ag nanodisc shows the plasmonic resonant peaks at which the electric field distributions, as well as the plasmonic dispersion relationship both clearly exhibit the characteristics of the plasmonic breathing modes.

Conclusion: We expect that the method that we have proposed, due to operating conveniently in the manner of far field excitation, will open many possibilities in practical applications based on the interaction between a single metal nanodisc with the radially polarized optical beam or between a metal nanodisc array with the beam array.

Keywords: Surface plasmon, Plasmonic breathing mode, Radially polarized optical beam, Metallic nanodisc

Background

As predicted [1], the plasmonics of metallic nanostructures remain a robustly growing research theme, as reflected, for instance, in the fast progress of quantum plasmonics [2], plasmon-induced hot carrier science and technology [3], and plasmon-enhanced Raman spectroscopy [4]. Among the many forms of metallic nanostructures [5], nanodiscs stand out as a very useful model for studying plasmonic properties. A metal nanodisc not only allows the coexistence of plasmonic resonances at all dimension levels, i.e., the volume, surface, and edge plasmonics [6, 7] but also possesses various types of surface plasmonic modes with well-defined two dimensional symmetries [8–10], in particular the interesting case of the plasmonic breathing modes [6, 7, 10].

The plasmonic breathing (PB) modes of a metal nanodisc are very special in the sense that they are radially symmetric and correlate with the intriguing collective radial oscillation of free electrons. Their appearance was first revealed in an electron energy loss spectroscopy study [10]. Their excitation by optical methods was considered to be difficult, because they are categorized as the dark modes owing to the null net electric dipole moment. Therefore, a recent experimental study [11] that showed that these modes can be excited under the oblique illumination of a linear polarized optical beam with the help of the retardation effect is notable. However, under this excitation approach, the PB modes are only weakly excited compared with the dominant plasmonic dipolar mode. Moreover, the other high-order plasmonic modes such as quadrupole and hexapole modes are also excited, which could overlay the PB modes. These situations were similarly encountered in the previous studies of optically excitation of the plasmonic dark modes

Li *et al. Journal of the European Optical Society-Rapid Publications* (2017) 13:23

Page 2 of 7

based either on using the symmetry-breaking nanostructures or on employing the retardation effect [12, 13].

Considering the unique symmetry and the low radiation loss of a dark mode [14–16], it will be desirable to exclusively and efficiently excite the PB modes with an optical method, which will certainly boost the application of metal nanodiscs in research fields such as surface enhanced Raman scattering, plasmonic lasing, localized refractive index sensing [17], local heating [18], and plasmonic trapping [19].

In this paper, we carry out a finite element method (FEM) numerical investigation to examine the interaction of an Au or an Ag nanodisc with two counter-propagating, radially polarized optical (RPO) beams. We find that only the PB modes will be excited if the axis of the incident beams coincides with that of the nanodisc. We systemically studied the near-field spectra, the electric field distributions correlated with the PB modes, and the dispersion relationship of these modes. To the best of our knowledge, such clear identification and detailed characterizations for exciting this type of mode with the RPO beam have not been reported. Previously, there were a few related demonstrations that either proved that the radially pointed plasmonic dark modes of the specifically patterned metal nanoparticle assembles can be excited by the RPO beam [20–22] or showed that the angular momentum is conserved when the high-order plasmonic modes of a metal nanodisc are excited by a focused optical vortex beam [23].

Methods

We performed the FEM simulation in the Comsol Multiphysics software under the geometry configuration displayed in Fig. 1(a). For simplicity, an isolated metal nanodisc in vacuum is considered. As we focused on the situation where the axis of the RPO beam coincides with that of the metal nanodisc (defined as the z-axis), the 2D rotationally symmetric model was applied. In our simulation, the RPO beam is created according to the paraxial expression given by

$$\overrightarrow{E} = E_0 \frac{\pi w_0 r}{w_1^2} GW \exp(-ikz + iwt)\overrightarrow{e_r},$$

$$\text{with } w_1 = w_0 \sqrt{1 + \left(\frac{z}{z_0}\right)^2},$$

$$G = \exp\left(-\frac{r^2}{w_1^2}\right),$$

$$W = \exp\left[\frac{-ikzr^2}{2(z_0^2 + z^2)} - i2\operatorname{atan}\left(\frac{z}{z_0}\right)\right],$$

$$z_0 = \frac{\pi w_0^2}{\lambda},$$

(1)

where w_0 represents the beam waist located at $z = 0$, G is the Gaussian envelope form, and W is the overall phase term including the Guoy phase. This formula [24, 25] is derived by considering that the RPO beam is actually composed of a right circularly polarized optical vortex beam with the topological charge of +1 and a left circularly polarized optical vortex beam with the topological charge of −1. We set $E_0 = 1$ V/m, $w_0 = 10$ μm, and the incident wavelength λ to be variable. The typical shape of the RPO beam with the null electrical field at the axis can be visualized clearly in Fig. 1(a) (calculated at $\lambda = 532$ nm).
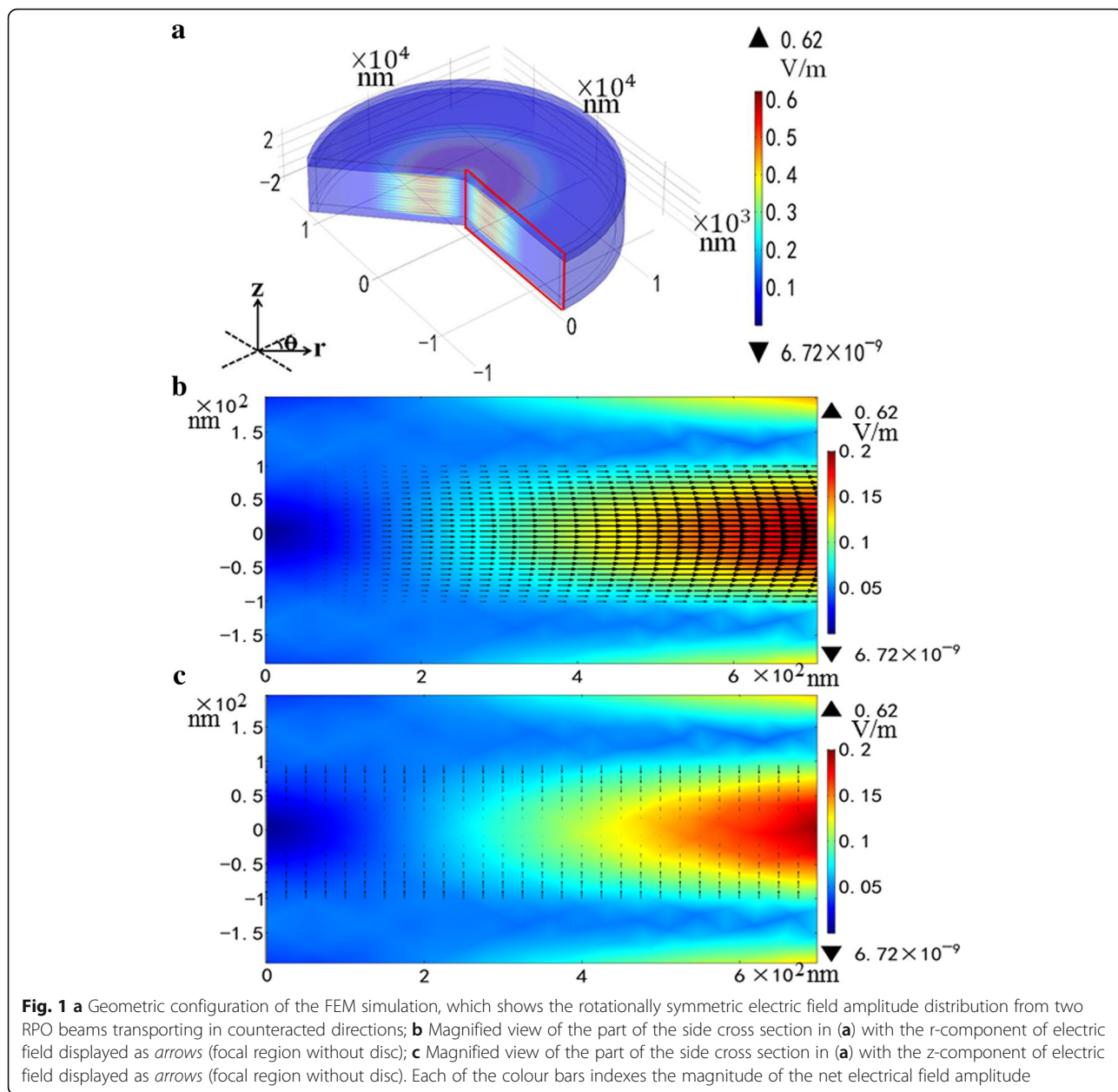
In our FEM simulation, we launched two RPO beams propagating face to face, as evidenced from the interference pattern shown on the side cross section of Fig. 1(a). This was done to obtain a volume zone containing zero z-component of electrical field (E_z) so that a metal nanodisc can be contained there and the condition for the interaction with a pure radial polarized electrical field can be fulfilled. We found that the above condition cannot be achieved by launching only one RPO beam: the electrical field always has some z-component even at the beam axis (which actually agrees with the theoretical prediction [26, 27]). Figure 1(b) and 1(c), respectively, plot the magnified views of the electrical field distributions E_r (r-component of the electrical field) and E_z at the neighbouring area of the rotational axis and $z = 0$ plane. Obviously, there is a zone of approximately 20 nm height satisfying $E_z = 0$ (in both figures, the colour background show the amplitude of the net electrical field). Therefore, we confined our study to the metal nanodisc with the thickness of 10 nm and with its mirror symmetrical plane on the $z = 0$ plane such that only E_r is effective in exciting the PB modes of the nanodisc. Note that the total incident optical beam now has the symmetry of the point group $D_{\infty h}$, the same as the nanodisc, whereas the single RPO beam can only be described by the point group $C_{\infty v}$.

Results and discussion

We first considered the Au-nanodiscs with various diameters. To follow the scaling law already demonstrated for the PB modes [7, 10], we varied the set diameters as $d = 1200$ nm, 600 nm, 400 nm, and 300 nm. To represent real conditions, we have used the Au dielectric functions reported by Johnson and Christy [28].

Figure 2 shows the results of the near-field spectra taken at the spatial point located on the Au-nanodisc axis and 2 nm above the nanodisc. Figure 2(a) plots the electric field amplitude $|E|$ versus λ the wavelengths of the incident RPO beam, Fig. 2(b) plots the phase ϕ versus λ, while the table in Fig. 2(c) lists all λ correlated to the surface plasmonic resonance (SPR) peaks appearing in Fig. 2(a) and zero-phase points in Fig. 2(b).
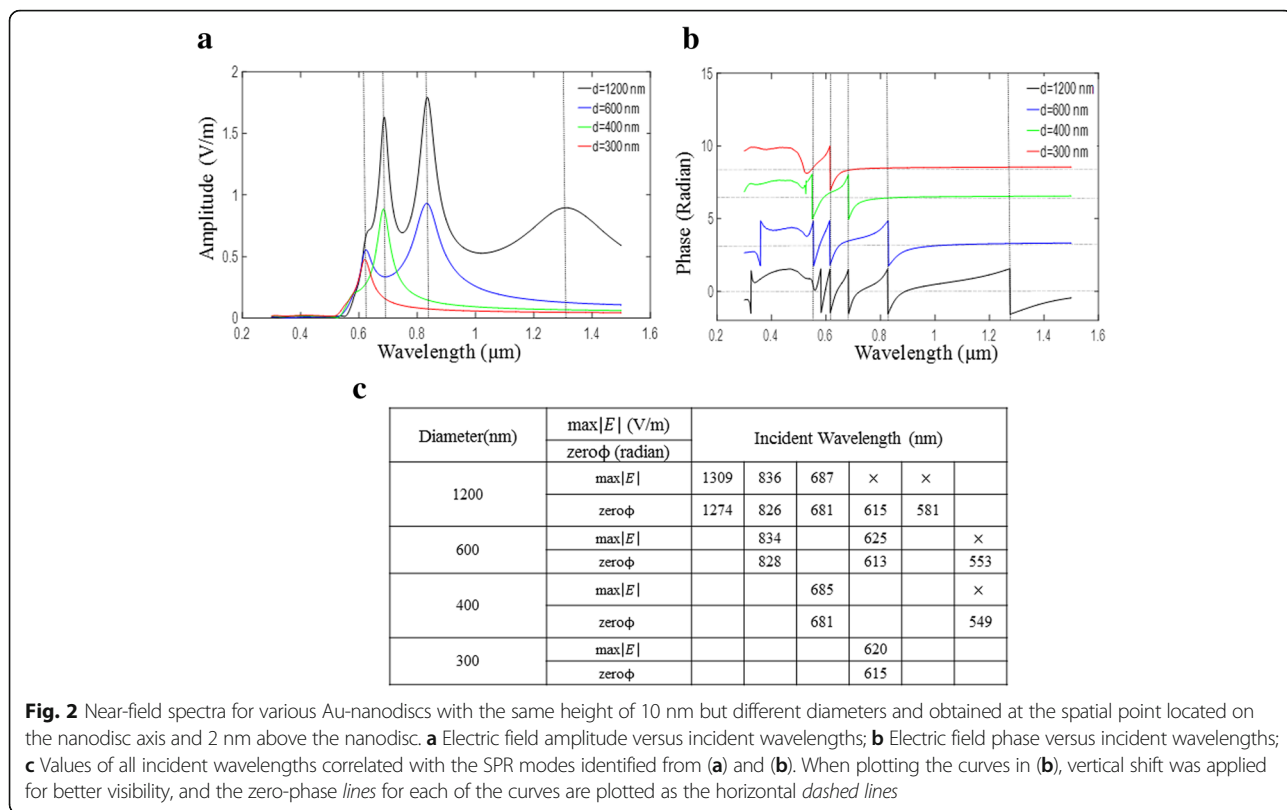
As shown in Fig. 2(a), for the 1200 nm Au-nanodisc, there are clear three SPR peaks, whereas two peaks are

Li *et al. Journal of the European Optical Society-Rapid Publications* (2017) 13:23

Page 3 of 7

Fig. 1 a Geometric configuration of the FEM simulation, which shows the rotationally symmetric electric field amplitude distribution from two RPO beams transporting in counteracted directions; **b** Magnified view of the part of the side cross section in (**a**) with the r-component of electric field displayed as *arrows* (focal region without disc); **c** Magnified view of the part of the side cross section in (**a**) with the z-component of electric field displayed as *arrows* (focal region without disc). Each of the colour bars indexes the magnitude of the net electrical field amplitude

observed for the 600 nm Au-nanodisc and single peaks are observed for both 400 nm and 300 nm Au-nanodiscs. Going from the long λ to short λ (i.e., from low energy to high energy), it is obvious that the first SPR peak of the 600 nm Au-nanodisc coincides with the second SPR peak of the 1200 nm Au-nanodisc, the first SPR peak of the 400 nm Au-nanodisc coincides with the third SPR peak of the 1200 nm Au-nanodisc, and the first SPR peak of the 300 nm Au-nanodisc coincides with the second SPR peak of the 600 nm. These results clearly manifest the scaling law, which states that the SPR wavelengths λ_{SPR} of the PB modes scale with the nanodisc diameter according to [7, 10].

$$\lambda_{SPR} = d/n, \text{ with } n = 1, 2, 3... \tag{2}$$

Figure 2(b) shows more interesting phenomena. The phase curves exhibit a series of π abrupt phase jumps near the SPR peaks shown in Fig. 2(a). This is actually in agreement with the criterion for characterizing a general resonance [29]. Now, the fourth and the fifth SPR peaks of the 1200 nm Au-nanodisc, the third peak of the 600 nm Au-nanodisc, and the second peak of the 400 nm Au-nanodisc, which are all barely visible in Fig. 2(a), can be easily identified. From Fig. 2(c), we can see that each of the SPR phase jumps λ (same as the zero-phase λ) is blueshifted relative to the corresponding SPR

Diameter(nm)	max|E| (V/m) / zeroφ (radian)	Incident Wavelength (nm)					
1200	max|E|	1309	836	687	×	×	
	zeroφ	1274	826	681	615	581	
600	max|E|		834		625		×
	zeroφ		828		613		553
400	max|E|			685			×
	zeroφ			681			549
300	max|E|				620		
	zeroφ				615		

Fig. 2 Near-field spectra for various Au-nanodiscs with the same height of 10 nm but different diameters and obtained at the spatial point located on the nanodisc axis and 2 nm above the nanodisc. **a** Electric field amplitude versus incident wavelengths; **b** Electric field phase versus incident wavelengths; **c** Values of all incident wavelengths correlated with the SPR modes identified from (**a**) and (**b**). When plotting the curves in (**b**), vertical shift was applied for better visibility, and the zero-phase *lines* for each of the curves are plotted as the horizontal *dashed lines*

amplitude peak λ. From the data presented in this table, it is easy to deduce that the scaling law of Eq. (2) holds for all SPR modes defined by the SPR phase jumps.

To confirm that the SPR modes excited by the RPO beam are indeed the PB modes, we then computed their electric field distributions. Several examples are displayed in Fig. 3. Figure 3(a)-(d) show the $n = 4, 3, 2, 1$ SPR modes for the 1200 nm Au-nanodisc, while Fig. 3(e) shows the $n = 2$ SPR mode for the 600 nm Au-nanodisc and Fig. 3(f) shows the $n = 1$ SPR mode for the 300 nm Au-nanodisc. Here, we illustrate the various SPR modes excited for a same Au-nanodisc using Fig. 3(a)-(d), and compare the SPR modes for a different Au-nanodisc excited at a same incident wavelength using Fig. 3(a), (e), and (f).

In each of these figures, the coloured background draws the snapshot of E_z and the distributed arrows illustrate the snapshot of $\vec{E}$. Here, the electrical field takes the normalized value, with the normalization obtained by dividing with $|E_r|$ of the RPO beam at the spatial point 2 nm away from the edge of each Au-nanodisc. We note that by using such normalization, the resultant value of E_z and the arrow length of $\vec{E}$ both clearly reflect the enhancement factor and the excitation efficiency of these SPR modes excited by the RPO beam. At first glance, all electric field distributions display the apparent mirror symmetry with their vector nature. As the surface charge density is

determined by E_z at the surface (and the sign is determined by whether the direction of E_z is pointed outwards from the nanodisc), the surface charge distribution thus also shows mirror symmetry. Adding the radial symmetry, these symmetric properties fit well with the fingerprints of the PB modes.

Close examination of the electrical field distributions shown in Fig. 3(a)-(d) reveals their respective E_z patterns on the Au-nanodisc surface show 4, 3, 2, and 1 nodes, which well characterize the first four PB modes of the 1200 nm Au-nanodisc. These patterns also show the similarity to the zero-order Bessel functions. Inspection of Fig. 3(a), (e), and (f) shows that their respective E_z patterns show 4, 2, 1 nodes. As the modes in these three figures are excited at the same incident wavelength, they should have the same λ_{SPR} (considering the same dispersion relationship they should follow [7, 10]), and the scaling law of Eq. (2) is clearly verified once again. Finally, we can also compare Fig. 3(e) with Fig. 3(c) and (f) with Fig. 3(d), so that we can observe that the PB modes with the same index are merely rescaled by the changes in the nanodisc diameter.

It is then intriguing to further investigate whether these PB modes follow the dispersion relationship of the antisymmetric film surface plasmon (FSP) as has been claimed previously [7, 10]. The results are displayed in Fig. 4. Here, the discrete data points are plotted according to the values listed in the table of Fig. 2. The SPR
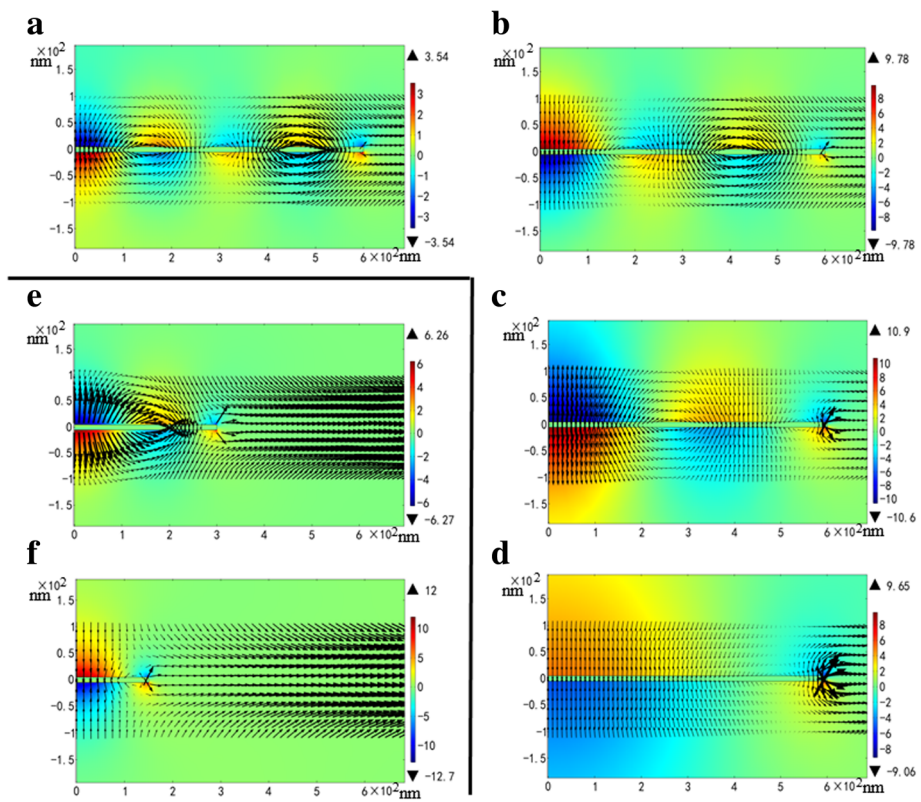
Li *et al. Journal of the European Optical Society-Rapid Publications* (2017) 13:23

Page 5 of 7

Fig. 3 Examples of computed electrical field distributions of the PB modes excited by the RPO beam (the electrical field is given in the normalized values by dividing with the electrical field amplitude of the incident beam at the point 2 nm away from the edge of each nanodisc). **a-d** PB modes of the 1200 nm Au-nanodisc excited at the incident wavelengths of 0.619 μm, 0.684 μm, 0.8304 μm and 1.291 μm, respectively. **e-f** PB modes excited at the incident wavelength of 0.619 μm for the 600 nm Au-nanodisc and the 300 nm Au-nanodisc, respectively. As can be determined in Fig. 2(c), all of these wavelengths are slightly larger than the zero phase wavelengths. From (**a**)-(**f**), the arrows are plotted with the relative length scale of 1:1:1:1.5:1:0.5 (the smaller scale means that the same length represents smaller electrical field amplitude)

energy is calculated as $hc/(\lambda e)$, and the SPR wavenumber takes the value of $2\pi/\lambda_{SPR}$ with λ_{SPR} determined by Eq. (2). The dispersion curve shown by the solid line is the result of the antisymmetric FSP calculated for the 10 nm thick Au film using [30, 31]:

$$\tanh(k_1) = -(k_1\varepsilon_2)/(k_2\varepsilon_1), \text{ with } k_i^2 = \beta^2 - k_0^2\varepsilon_i, \quad (3)$$

where β is the SPR wavenumber, k_0 is the incident wave wavenumber, ε_1 is the dielectric function of Au [28], and $\varepsilon_2 = 1$ is the dielectric constant of air. Here, the red dots represent the first five PB modes of the 1200 nm Au nanodisc, and the blue dot represents the third PB mode of the 600 nm Au nanodisc (the zero phase λ are used, as shown in Fig. 2(c) table). The data points for the other PB modes listed in Fig. 2(c) table will overlay with these red dots or the blue dot. Therefore, all obtained PB modes tightly follow the dispersion relationship of the Au antisymmetric FSP.

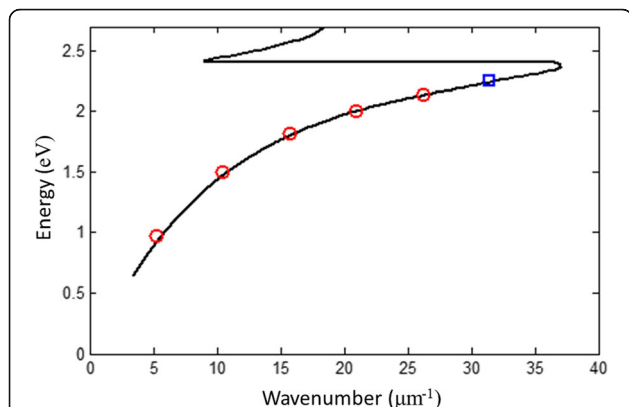Finally, we also endeavoured to perform a similar systemic study on the 10 nm thick Ag nanodiscs. The

Fig. 4 Dispersion relationship of the PB modes compared with the dispersion curve of the antisymmetric FSP. *Red* and *blue dots* represent PB modes of the 10 nm thick Au-nanodiscs

Li *et al. Journal of the European Optical Society-Rapid Publications* (2017) 13:23

Page 6 of 7

results of the near field spectrum of the 1200 nm Ag nanodisc and the dispersion relationship of its PB modes are both plotted in Fig. 5. The Ag dielectric function from [28] is also applied. As seen, the obtained results are consistently similar to those obtained for the Au nanodisc.

In our current simulation, we considered the ideal simplified case that the RPO beam is not tightly focused. As the beam waist must be set to be much larger than the incident wavelength to satisfy the paraxial transport condition, the total portion of the light energy utilized to excite the PB modes of the metal nanodisc is limited. However, our intention here is to show the first step to prove that the pure radially pointed electrical field of the RPO beam can efficiently excite the PB modes where the excitation efficiency is defined relative to the beam intensity at the point close to the nanodisc edge instead of

to the maximum intensity across the whole beam. We will extend our study to the more practical case with the focused RPO beam in the next report where the effects of E_r and E_z on the PB mode excitation both need to be taken into account. Moreover, we will also upgrade to a 3-dimensional model, which allows us to investigate other realistic conditions such as the case when a supporting dielectric layer for the metal nanodisc is present, when the RPO beam is not perfectly aligned with the metal nanodisc and when the metal nanodisc is not perfectly shaped as a circle.

Conclusions

To summarize, we proposed the use of radially polarized optical vector beams to excite the plasmonic breathing modes of a metal nanodisc and confirmed this capability through the finite-element method simulation. The near
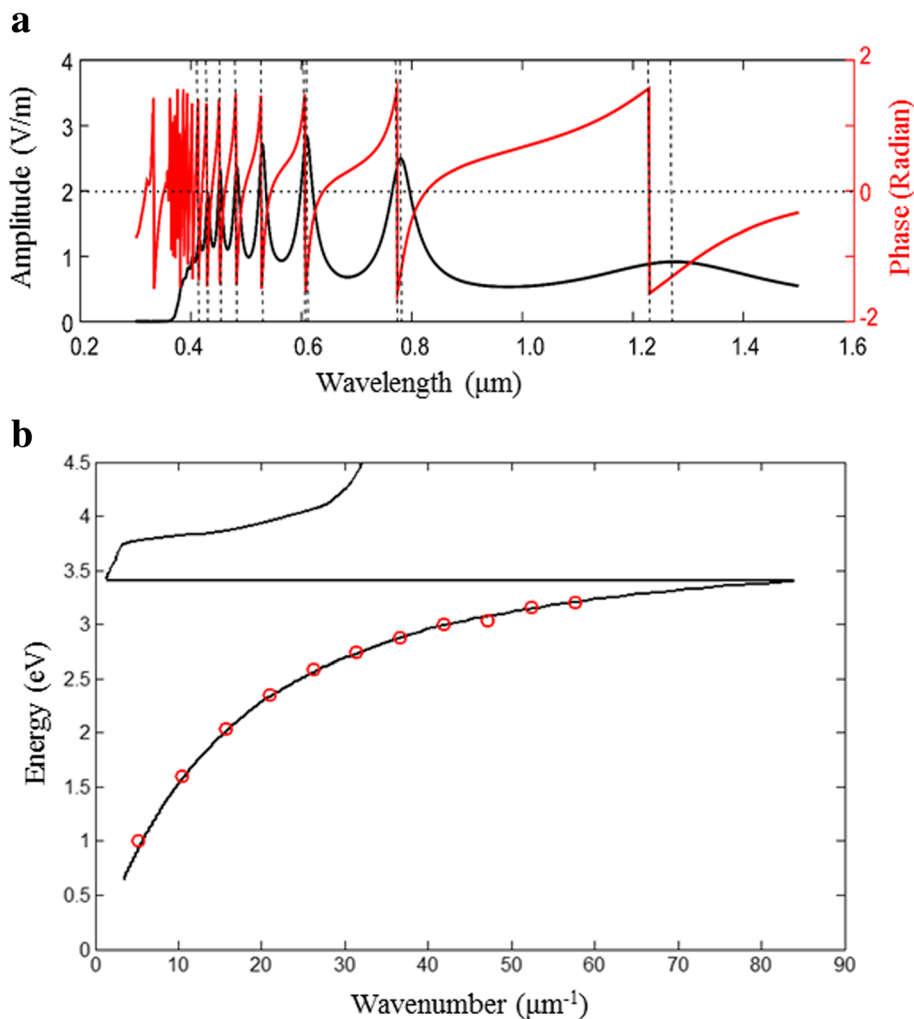

Fig. 5 Simulated results for the 10 nm thick Ag nanodisc with the diameter of 1200 nm. **a** Near-field spectrum taken at the spatial point located on the nanodisc axis and 2 nm above the nanodisc. **b** Dispersion relationship of the PB modes compared with the dispersion curve of the antisymmetric FSP

Li *et al. Journal of the European Optical Society-Rapid Publications* (2017) 13:23

Page 7 of 7

field spectra and the dispersion relationships presented in Figs. 2, 4, and 5 strongly supported the scaling law given by Eq. (2) for the metal nanodisc PB modes. Accordingly, one of the unique advantages of applying the metal nanodisc in plasmonic studies is that the plasmonic resonant wavelengths of its plasmonic breathing modes can be predictably tuned by adjusting the nanodisc size. Considering the fast expansion of the research directed at the application of optical vector beams to interact with nanostructures [32], we believe that the method demonstrated here will facilitate the study of dark mode surface plasmonics and will be applied to some practical designs such as the metal nanodisc based gap mode surface enhance Raman scattering and tip enhance Raman scattering, and the metal nanodisc array based plasmonic trapping and heating.

Abbreviations
FEM: finite element method; FSP: film surface plasmon; PB: plasmonic breathing; RPO: radially polarized optical; SPR: surface plasmonic resonance

Availability of data and materials
Detail about data has been provided in the article.

Authors' contributions
Hui Fang proposed the original idea, guided the research and wrote the manuscript. Mengjun Li implemented the simulations and drafted the manuscript. Xiaoming Li was involved in some of the simulations. Xiaocong Yuan advised the research and revised the manuscript. All of the authors read and approved the final manuscript.

Ethics approval and consent to participate
Not applicable.

Consent for publication
Not applicable.

Competing interests
The author(s) declare(s) that they have no competing interests.

Publisher's Note
Springer Nature remains neutral with regard to jurisdictional claims in published maps and institutional affiliations.

Author details
[1]Institute of Modern Optics, College of Electronic Information and Optical Engineering, Nankai University, Tianjin 300071, China. [2]Nanophotonics Research Centre & Key Laboratory of Optoelectronic Devices and Systems of Ministry of Education and Guangdong Province, College of Optoelectronic Engineering, Shenzhen University, Shenzhen 518060, China.

References
1. Halas, NJ, "Plasmonics: An Emerging Field Fostered by Nano Letters," Nano Lett. **10**(10), 3816–3822(2010)
2. Tame, M.S, McEnery, KR, Ozdemir, SK, Lee, J, Maier, SA, Kim, MS: Quantum plasmonics. Nat. Phys. **9**, 329–340 (2013)
3. Brongersma, ML, Halas, N.J, Nordlander, P: Plasmon-induced hot carrier science and technology. Nat. Nanotechnol. **10**, 25–34 (2015)
4. Ding, SY, Yi, J, Li, JF, Ren, B, Wu, DY, Panneerselvam, R, Tian, ZQ: Nanostructure-based plasmon-enhanced Raman spectroscopy for surface analysis of materials. Nature Reviews Materials. **1**, 1–16 (2016)
5. Zhang, JX, Zhang, LD: Nanostructures for surface plasmons. Adv. Opt. Photon. **4**, 157–321 (2012)
6. Hobbs, RG, Manfrinato, VR, Yang, YJ, Goodman, SA, Zhang, LH, Stach, EA, Berggren, KK: High-energy surface and volume plasmons in nanopatterned sub-10 nm aluminum nanostructures. Nano Lett. **16**, 4149–4157 (2016)
7. Schmidt, FP, Ditlbacher, H, Hohenester, U, Hohenau, A, Hofer, F, Krenn, JR: Universal dispersion of surface plasmons in flat nanostructures. Nat. Commun. **5**, 3604 (2014)
8. Schmidt, FP, Ditlbacher, H, Hofer, F, Krenn, JR, Hohenester, U: Morphing a plasmonic nanodisk into a nanotriangle. Nano Lett. **14**, 4810–4815 (2014)
9. Imura, K, Ueno, K, Misawa, H, Okamoto, H, McArthur, D, Hourahine, B, Papoff, F: Plasmon modes in single gold nanodiscs. Opt. Express. **22**, 12189–12199 (2014)
10. Schmidt, FP, Ditlbacher, H, Hohenester, U, Hohenau, A, Hofer, F, Krenn, JR: Dark plasmonic breathing modes in silver nanodisks. Nano Lett. **12**, 5780–5783 (2012)
11. Krug, MK, Reisecker, M, Hohenau, A, Ditlbacher, H, trugler, A, Hohenester, U, and Krenn, JR: "Probing plasmonic breathing modes optically," Applied Physics Letters **105**, 171103 (2014)
12. Hao, F, Sonnefraud, Y, Dorpe, PV, Maier, SA, Halas, N.J, Nordlander, P: Symmetry breaking in plasmonic nanocavities: subradiant LSPR sensing and a tunable Fano resonance. Nano Lett. **8**, 3983–3988 (2008)
13. Hao, F, Larsson, EM, Ali, TA, Sutherland, DS, Nordlander, P: Shedding light on dark plasmons in gold nanorings. Chem. Phys. Lett. **458**, 262–266 (2008)
14. Liu, MZ, Lee, TW, Gray, SK, Sionnest, PG, Pelton, M: Excitation of dark plasmons in metal nanoparticles by a localized emitter. Phys. Rev. Lett. **102**, 107401 (2009)
15. Chen, HY, He, CL, Wang, CY, Lin, MH, Mitsui, D, Eguchi, M, Teranishi, T, Gwo, S: Far-field optical imaging of a linear array of coupled gold nanocubes: direct visualization of dark plasmon propagating modes. ACS Nano. **10**, 8223–8229 (2011)
16. D. Solis Jr, Willingham, BSL L, Nauert, LS, Slaughter, J, Olson, P, Swanglap, A, Paul, WS, Chang, and Link, S: "Electromagnetic energy transport in nanoparticle chains via dark plasmon modes," Nano Letter **12**, 1349–1353 (2012)
17. Hafele, V, Trugler, A, Hohenester, U, Hohenau, A, Leitner, A, Krenn, JR: Local refractive index sensitivity of gold nanodisks. Opt. Express. **23**, 10293–10300 (2015)
18. Donner, JS, Baffou, G, McCloskey, D, Quidant, R: Plasmon-assisted optofluidics. ACS Nano. **7**, 5457–5462 (2011)
19. Righini, M, Volpe, G, Girard, C, Petrov, D, Quidant, R: Surface plasmon optical tweezers: tunable optical manipulation in the femtonewton range. Phys. Rev. Lett. **100**, 186804 (2008)
20. Paramon, JS, Bosch, S: Dark modes and Fano resonances in plasmonic clusters excited by cylindrical vector beams. ACS Nano. **9**, 8415–8423 (2012)
21. Gomez, DE, Teo, ZQ, Altissimo, M, Davis, TJ, Earl, S, Roberts, A: The dark side of plasmonics. Nano Lett. **13**, 3722–3728 (2013)
22. Yanai, A, Grajower, M, Lerman, GM, Hentschel, M, Giessen, H, Levy, U: Plasmonic oligomers under radially and azimuthally polarized light excitation. ACS Nano. **8**, 4969–4974 (2014)
23. Sakai, K, Nomura, K, Yamamoto, T, Sasaki, K: Excitation of multipole plasmons by optical vortex beams. Sci Rep. **5**, 8431 (2015)
24. Andrews, DL, Babiker, M: Eds, the Angular Momentum of Light (Cambridge University Press, 2013)
25. Zhan, QW: Cylindrical vector beams: from mathematical concepts to applications. Adv. Opt. Photon. **1**, 1–57 (2009)
26. Herrero, RM, Mejias, PM: Propagation of light fields with radial or azimuthal polarization distribution at a transverse plane. Opt. Express. **16**, 9021–9033 (2008)
27. Kotlyar, VV, Kovalev, AA: Nonparaxial propagation of a Gaussian optical vortex with initial radial polarization. J. Opt. Soc. Am. A. **27**, 372–380 (2010)
28. Johnson, PB, Christy, RW: Optical constant of nobel metals. Phys. Rev. B. **6**, 4370–4379 (1972)
29. Joe, YS, Satanin, AM, Kim, CS: Classical analogy of Fano resonances. Phys. Scr. **74**, 259–266 (2006)
30. Maier, SA: Plasmonics: Fundamentals and Applications (Springer, 2007)
31. Dionne, JA, Sweatlock, LA, Atwater, HA: Planar metal plasmon waveguides: frequency-dependent dispersion, propagation, localization, and loss beyond the free electron model. Phys. Rev. B. **72**, 075404 (2005)
32. Wozniak, P, Banzer, P, Leuchs, G: Selective switching of individual multipole resonances in single dielectric nanoparticles. Laser Photonics Rev. **9**, 231–240 (2015)